



The influence of anion-exchange membrane nanostructure onto ion transport: Adjusting membrane performance through fabrication conditions

Lukas Fischer^{a,b}, Sven Sören Hartmann^c, Artjom Maljusch^c, Christian Däschlein^c, Oleg Prymak^d, Mathias Ulbricht^{a,b,*}

^a Lehrstuhl für Technische Chemie II and Center for Nanointegration Duisburg-Essen (CENIDE), University Duisburg-Essen, Universitätsstr. 5, 45141, Essen, Germany

^b NETZ-NanoEnergieTechnikZentrum, University Duisburg-Essen, Carl-Benz-Str. 199, 47057, Duisburg, Germany

^c Evonik Operations GmbH, CREAVIS, Paul-Baumann-Str. 1, 45772, Marl, Germany

^d Inorganic Chemistry and Center for Nanointegration Duisburg-Essen (CENIDE), University Duisburg-Essen, Universitätsstr. 5, 45141, Essen, Germany

ARTICLE INFO

Keywords:

Anion-exchange membrane
Self-assembly
Ion transport mechanism
Diffusion dialysis
Ionic conductivity

ABSTRACT

We fabricated dense anion-exchange membranes from the same polymer with variations in the self-assembled hydrophilic and hydrophobic domains. We show how the nanostructure forms during membrane formation and how it can be tuned by rationally designing fabrication conditions. We found that the hydrophilic and hydrophobic domain structure evolves during the membrane solidification. This can be controlled by using casting solvents with different evaporation times or by the addition of an ionic liquid which alters the interactions in the polymer film. We could further tailor the structure of solidified membranes by heat or solvent annealing and developed conditions that selectively adjust the nanostructure in different parts of the membrane. With these methods we could significantly optimize the macroscopic properties and ion transport rates of membranes made from the same polymer. The ionic liquid additive led to an almost doubling of the water uptake without influencing the swelling degree and also to a 3-fold higher diffusion rate for HBr. By using a post-treatment with dioxane we also managed to fabricate a membrane with a 5-fold higher ionic conductivity. We further found that different transport mechanisms are involved in ionic conductance and acid diffusion and could relate them to different membrane nanostructures.

1. Introduction

Anion-exchange membranes (AEMs) are of high interest because of their use in promising renewable energy and environmental waste management technologies [1–3]. For example, the synthesis of hydrogen by water electrolysis is still more expensive than from natural gas sources which hinders the industrial implementation [4]. One very promising approach to reduce the cost of green hydrogen production is the use of AEMs as solid electrolyte in alkaline water electrolyzers as they can be combined with cheap non-precious metals as catalysts [5]. For this, the achievable ionic conductivity of AEMs directly correlates to the hydrogen production rates and energy efficiency; however, so far the performance of commercial membranes still limits the widespread application. AEMs are also an interesting option to recycle acids from wastes that are produced in metal finishing industries [6]. By using AEM-enabled diffusion dialysis, acids can be transported from the feed

into the permeate compartment, while positively charged metal ions are held back via Donnan exclusion. This results in an environmentally friendly and low energy consuming upcycling of industrial wastes, but the selectivity and acid diffusion rates of available membranes are not sufficient for a large-scale application [7].

Most approaches to increase anion-exchange membrane performance are based on the synthesis of new polymers, with focus on altering the chemical functionalities or polymer architecture [8–16]. However, recently more and more research showed the importance of the nanoscale morphology to control membrane performance [17–24]. AEMs, like most ion-exchange membranes, are usually fabricated by film casting of a charged ionomer in solution and subsequent solvent evaporation, leading to dense and isotropic polymer films. During the evaporation step, the charged side chains and the hydrophobic backbone, respectively, can assemble into larger clusters resulting in the formation of hydrophilic and hydrophobic domains in the nano-

* Corresponding author. Lehrstuhl für Technische Chemie II and Center for Nanointegration Duisburg-Essen (CENIDE), University Duisburg-Essen, Universitätsstr. 5, 45141, Essen, Germany.

E-mail address: mathias.ulbricht@uni-essen.de (M. Ulbricht).

<https://doi.org/10.1016/j.memsci.2022.121306>

Received 12 October 2022; Received in revised form 29 November 2022; Accepted 21 December 2022

Available online 27 December 2022

0376-7388/© 2022 The Authors. Published by Elsevier B.V. This is an open access article under the CC BY license (<http://creativecommons.org/licenses/by/4.0/>).

microscale [25]. This alignment of the different parts of the polymer is influenced by the solvent-polymer and polymer-polymer interactions as well as the drying temperature which all contribute to the thermodynamic and kinetic parameters of this nanophase segregation [26–28]. For example, Akhtar et al. showed that the same ionomer can be fabricated into different cation-exchange membranes which have a changed nanoscale morphology dependent on the used casting solvent and the resulting membranes also showed significant differences in water vapor permeance [29]. Even after the solidification process the membrane structure can still be altered through heat or chemical treatment. It was shown that treating different anion-exchange membranes at elevated temperatures leads to a change of the macroscopic structural properties [30]. Similarly, Safronova et al. showed that the ionic conductivity of cation-exchange membranes can be altered by heat treatment [31]. It was also already observed that a solvent post-conditioning influenced the conductivity and salt diffusion rates of different cation- and anion-exchange membranes [32]. Still, however, no systematic investigation of a wide range of fabrication conditions and the underlying mechanisms of structural change was done yet. Furthermore, while the relationship between nanostructure and ion transport is often discussed, no clear statement regarding the optimal morphology and its influence on the transport mechanism can be made [33–38]. There are mainly two models regarding the transport through dense ion-exchange membranes. One of the leading theories is that the nanophase segregation results in an interstitial phase throughout the membrane, allowing for the formation of connected water pathways [39]. This means that also the ionic flux through the membrane can be completely described by the extended Nernst-Planck equation, and the polymer does not directly participate in the ion transport [40]. Another model describes the formation of hydrophilic regions as charged nanochannels, in which the transport of ions is facilitated by the hopping mechanism, i.e. ions jumping between neighboring charged groups that are part of the polymer structure [41].

Establishing a relationship between membrane fabrication and the resulting nanostructure as well as correlating the nanostructure to the transport properties would allow for new membrane designs. Therefore, in this study we used several fabrication conditions to synthesize anion-exchange membranes from the same polymer that show significant differences in their nanoscale morphology. By analyzing the formed hydrophilic domains via atomic force microscopy (AFM) and small angle x-ray scattering (SAXS) we related the nanostructure to the underlying processes during membrane formation and showed how these processes can be controlled through varied conditions. We further measured the diffusion rates for several acids and the ionic conductance. Comparing the results of these measurements allowed us to make relevant statements regarding the involved transport mechanisms and to establish a blueprint on how to tune ion-exchange membranes towards higher ion transport performance.

2. Materials and methods

2.1. Fabrication of membranes

2.1.1. Solvent selection for membrane fabrication

The anion-exchange polymer for this study was provided by Evonik Operations GmbH. The Hansen solubility parameters for the polymer were determined by a commercial provider. To find solvents for the polymer with different boiling points for film casting, single solvents and binary solvent mixtures were screened for their relative energy difference (RED) value via HSPiP software [42]. For selected solvent systems with low RED value solubility tests were conducted with 25 wt% polymer. For binary solvent mixtures that dissolved the polymer, the evaporation behavior was calculated via Raoult's law to determine a temperature where the mixture shows azeotropic evaporation. To adjust for non-ideal solutions, the activity coefficients were calculated via the Wilson parameters and the infinite dilution activity coefficients [43,44].

As a result, dimethylsulfoxide (DMSO) was determined as suitable high boiling point solvent, and acetonitrile/ethanol (ACN/EtOH) (56/44 w %) was identified as low boiling point solvent with a uniform evaporation behavior between 50 and 60 °C.

2.1.2. Casting solution and membrane preparation

The anion-exchange polymer (26% w/v) was dissolved in the corresponding solvent, optionally also containing an additive, and the resulting solution was stirred for 24 h at room temperature (Table 1). The casting solutions were degassed at 200 mbar for 10 min and subsequently casted on glass to 500 µm thick films at a relative humidity of 20%. Afterwards, the films were dried, and final membranes were stored in water.

2.1.3. Post-treatment

Pieces of the final membrane CC-DMSO were cut out and incubated in either acetone (CC-DMSO-Acetone) or 1,4-dioxane (CC-DMSO-Dioxane) at room temperature, or in dry state at 60 °C (CC-DMSO-60 °C) for 7 days. Afterwards the membrane pieces were washed and stored in water.

2.2. Membrane characterization

2.2.1. Water uptake and swelling degree

Samples of 16 mm diameter were cut out of all fabricated membranes and were incubated in water for 24 h at 60 °C. Subsequently samples were weighed, and their thickness and diameter were measured. Afterwards, the samples were dried at 60 °C for 24 h and weight, thickness and diameter were determined in dry state. The water uptake was calculated as percentage of weight increase after water uptake, the swelling degree was the percentage the thickness increased in wet state, and from weight, thickness and diameter in dry state the density of the membranes was calculated.

2.2.2. Transmission electron microscopy

Transmission electron microscopy (TEM) analysis was performed for membrane CC-DMSO (1) to test the suitability of this method. The membrane was beforehand stained in a 2 M NaI solution for 24 h on a shaker and afterwards washed three times with DI water and dried [45]. The membrane was fixated in an epoxy resin and cut with a EM UC7/FC7 microtome from Leica. TEM images were obtained using a JEOL 2200FS instrument (see Figs. S1–S2 in SI).

2.2.3. Atomic force microscopy

To investigate the resulting nanoscale morphology, AFM analysis of all fabricated membranes was done in dry and wet state with a Bruker Dimension FastScan® system using PeakForce Tapping® to obtain topographic images. Images of 500 × 500 nm² were used to analyze the morphology of membranes via the image analyzer software ImageJ. To quantify the average area and overall surface fraction of hydrophilic regions, two-dimensional images were loaded into the program, converted to 8-bit and subjected to the Threshold method (Default), followed by using the Particle Analyzer (see Figs. S3–S9 and Table S1 in SI).

Table 1

Conditions used to prepare casting solutions for film casting and subsequent drying.

Membrane	Solvent	Additive	Drying
CC-DMSO	DMSO	–	60 °C, 24 h
CC-DMSO-IL	DMSO	5 v% 1-Butyl-3-methylimidazolium acetate	60 °C, 24 h
CC-ACN/EtOH	ACN/EtOH (56/44 w%)	–	60 °C, 24 h
CC-ACN/EtOH-Aq	ACN/EtOH (56/44 w%)	6 v% Water	60 °C, 24 h

2.2.4. Small-angle X-ray scattering

SAXS was used to investigate the nanoscale ordering through the whole membrane for fabricated AEMs. The measurements were performed on a Panalytical Empyrean diffractometer with Cu K α radiation (U = 40 kV and I = 40 mA, line focus) using an evacuated beam path chamber ScatterX-78 (vacuum 0.1 mbar) and a sample-to-detector distance of 240 mm (2D PIXcel3D detector). The membranes were fixed in a sample holder for transmission mode and measured in the 2 Θ range of -0.15° to $+5.00^\circ$ at a step size 0.01° leading to a total measurement time of 21 min. The scattering vector was calculated as follows:

$$q = 4\pi \sin\theta / \lambda \quad (1)$$

with λ the wavelength of the X-ray radiation ($\lambda = 1.54 \text{ \AA}$) and Θ the scattering angle. This enabled to reach the values of q between 0.012 and 0.35 \AA^{-1} , which corresponds to periodicities between 50 and 2 nm. The inter-domain distance d was calculated from the q value of determined SAXS peaks according to:

$$d = 2\pi / q \quad (2)$$

2.3. Membrane evaluation

2.3.1. Conductivity measurement

The through-plane conductivity was measured in a homemade conductivity cell (see Fig. S10 in SI). Membrane pieces (3.75 cm^2) were incubated in 1 M KOH for 24 h and afterwards clamped in the middle of the cell between two graphite electrodes. In this set-up, the membrane has no direct contact to the electrodes but is fully immersed in the electrolyte (1 M KOH). Electrochemical impedance spectroscopy was conducted by connecting both electrodes to a potentiostat (BioLogic VMP3) and a frequency sweep from 200 kHz to 100 Hz was used to obtain the Nyquist plot. The resistance of the analyzed system was gathered from the Nyquist plot and membrane resistance was calculated by subtracting the electrolyte only resistance from the resistance of electrolyte plus membrane. The specific ionic conductivity was calculated as follows:

$$\kappa = t / (R \cdot A) \quad (3)$$

with t membrane thickness, R membrane resistance and A membrane area.

2.3.2. Diffusion dialysis

To measure the diffusion rate of different acids through the fabricated membranes, a two-chamber diffusion cell was used (see Fig. S11 in SI). Membrane samples with a diameter of 30 mm were cut out and clamped between the permeate chamber with desalted water and the feed chamber with acid and both chambers were stirred rigorously to minimize concentration polarization. Before each measurement, membranes were conditioned by allowing dialysis with the respective acid for 30 min. The actual experiment started with addition of new water in the permeate chamber and new acid in the feed chamber. For the single acid measurements, the pH value of the permeate cell was measured over 30 min. The acid concentration in the permeate solution was calculated from the obtained pH values. The effective diffusion coefficients were calculated for each membrane and acid pair from Fick's first law. Plotting the acid concentration in the permeate vs. time showed a steady flux through the membrane during the investigated time period. The flux was obtained from the slope of the linear fit of the concentration vs. time data and diffusion coefficients were calculated using the initial concentration gradient of 1 mol/l (see Fig. S12 in SI). For the measurements with acid mixtures in the feed chamber, conditioning was done for 30 min with the same feed composition as used in the following measurement. The dialysis was conducted for 30 min and afterwards the concentrations of the acids in the permeate were analyzed via ion

chromatography using calibration curves (see Fig. S13 in SI).

3. Results and discussion

In this study we used a positively charged polymer with a not disclosed chemical structure to fabricate anion-exchange membranes (AEMs) via film casting and subsequent solvent evaporation. We developed methods to alter and control the membrane nanostructure and could tailor the macroscopic membrane properties as well as the ion transport rates. Our approach is independent of having access to the exact polymer specifications and thus offers a blueprint for the rational design and fabrication of membranes from commercial ionomers.

3.1. Fabrication conditions

Overall, we fabricated a library of seven AEMs from the same polymer with almost the same thickness. We used two different solvent systems to generate casting solutions, DMSO (CC-DMSO (1)) and acetonitrile/ethanol (CC-ACN/EtOH (3)). For both solvent systems we used the same drying temperature which resulted in different durations until the solvent evaporated and the membrane solidified. To alter the polymer-solvent and polymer-polymer interactions during the membrane formation, additives were used that remain in the membrane after the solvent has evaporated, namely the ionic liquid 1-butyl-3-methylimidazolium acetate (5 v%) as additive in DMSO (CC-DMSO-IL (2)) and water (6 v%) as additive in acetonitrile/ethanol (CC-ACN/EtOH-Aq (4)). To investigate a possible membrane annealing after fabrication, samples of CC-DMSO (1) were post-treated for 7 days in either the polar non-solvent acetone (PT-DMSO-Acetone (5)), the non-polar non-solvent 1,4-dioxane (PT-DMSO-Dioxane (6)) or at 60°C (PT-DMSO- 60°C (6)). These conditions were designed based on the Hansen Solubility Parameter (HSP) concept [42]. The HSP describe the ability of a molecule to interact via London dispersion forces (δ_D), dipolar intermolecular forces (δ_P) and hydrogen bonding (δ_H). Molecules with similar HSP can interact with each other, and values for the relative energy distance (RED) significantly lower than 1 indicate complete miscibility or solubility (Table 2).

Both casting solvent systems have RED values that correspond to a complete solvation of the polymer, while the non-solvents used for the post-treatment should not be able to dissolve the polymer (higher RED value). Regarding the HSP of the polymer, the amphiphilic structure means that the charged groups will mainly contribute to the high values of δ_P and δ_H (hydrophilic) and the backbone will mainly contribute to the high δ_D value (hydrophobic) [46]. This means that the non-polar 1,4-dioxane with low δ_P and high δ_D is more similar to the backbone, and that the moderately polar acetone with a higher δ_P and lower δ_D value is more similar to the charged side groups. As a result, the post-treatment solvents should only diffuse into and then anneal the corresponding hydrophobic or hydrophilic parts of the solidified membrane.

3.2. Morphology

After film casting and solvent evaporation the nanoscale morphology

Table 2

HSP values for the used anion-exchange polymer as well as casting and post-treatment solvents.

		δ_D (MPa $^{1/2}$)	δ_P (MPa $^{1/2}$)	δ_H (MPa $^{1/2}$)	RED
Casting solvents	Used polymer	18.6	13.7	11.4	–
	DMSO	18.4	16.4	10.2	0.36
	ACN/EtOH	15.5	14.0	12.0	0.76
Post-treatment solvents	Acetone	15.5	10.4	7.0	1.00
	1,4-Dioxane	17.5	1.8	9.0	1.50

of all obtained membranes was investigated by AFM (Fig. 1).

In the AFM image of the dry membrane CC-DMSO (1) the nanoscale ordering of the surface is only weakly visible (Fig. 1a, exemplary). The TEM images of membrane 1 did also not show any larger isolated regions after iodine staining (see Section S1 in SI). In contrast, when we conducted AFM of the wet membranes we could observe distinct round regions that stick out of the membrane surface, which is similar to the AFM images of other AEMs (Fig. 1b–h) [21]. This shows that the small hydrophilic domains that formed during membrane solidification can only be detected after they swell through water uptake. CC-DMSO (1) as the baseline membrane has hydrophilic domains with an average size of 291 nm². The faster evaporating solvent (3) led to a reduction in average area to 117 nm². This decrease indicates that during the membrane drying step the hydrophilic domains enlarge over time. Such a formation of larger regions over time was also observed for cation-exchange membranes that were annealed with solvent vapor after fabrication [47]. We were further able to inhibit this process by the addition of ionic liquid (2) to DMSO as casting solvent, which resulted in smaller hydrophilic domains (182 nm²) in comparison to membrane 1 without the additive. A possible explanation is that the repulsion between cationic polymer groups drives the enlargement of hydrophilic clusters until the solvent is evaporated and that the ionic liquid lowers the driving force for that process by compensating the charges in the domains. On the other hand, water as additive to ACN/EtOH (4) led to irregular distributed hydrophilic regions on the surface that could not be quantified by the image analysis algorithm we used. The observed assemblies could be the result of water nanodroplets that remain after solvent evaporation and locally attract or solvate charged side chains.

We could also change the morphology of our membranes after solidification. Treating membrane 1 with acetone (5) led to significantly larger hydrophilic domains of 578 nm². According to the HSP (Table 2), acetone results in a selective solvation of charged regions and subsequently to an increased mobility in these parts. The observed larger domains fit well to the proposed enlargement over time. We saw a

similar effect after the heat annealing for membrane 7 which resulted in an average size of 471 nm². This means that elevation of temperature to 60 °C led to more mobility in the hydrophilic parts which could be explained by a generally loose packing in these regions due to the high charge density. In contrast, the post-treatment with dioxane (6) had the opposite effect and reduced the average hydrophilic domain size to 116 nm². The low polarity of dioxane (Table 2) should result in an uptake into the hydrophobic bulk. An increased mobility in the amorphous matrix could lead to outside pressure on the static hydrophilic domains, forcing the charged groups towards closer contact and leading to smaller sizes.

For all membranes the surface coverage with hydrophilic domains lies between 25 and 27% with the exception of membrane 3 (17%) and membrane 6 (35%). For membrane 6 this is likely due to changes in the hydrophobic bulk as shown by the higher membrane density that will be discussed below (Table 3). The surface coverage with hydrophilic domains is calculated relative to the area of the hydrophobic bulk, and a higher membrane density indicates that the hydrophobic bulk occupies less space. The comparison between the other membranes shows that all conditions increased the surface coverage to almost the same value compared to the fast evaporating solvent (3), independent of the actual size of hydrophilic regions. Our explanation for this is that membrane 3 solidified before the phase segregation into hydrophilic domains was complete, which leads to a low surface coverage. After the completed phase segregation, the enlargement in the other membranes could be a result of the assembly of different hydrophilic domains to form larger regions without influencing the overall surface coverage.

We further conducted SAXS measurements to obtain morphology data for the whole membrane (Fig. 2). For all membranes we found a maximum peak at high scattering vectors (high-q) as well as a minimum peak at low scattering vectors (low-q), features which were similarly observed for other AEMs [22]. The exact origin of such SAXS intensities was investigated in detail by Konishi et al. by analyzing polymer films via different scattering methods. They could show that a peak in the

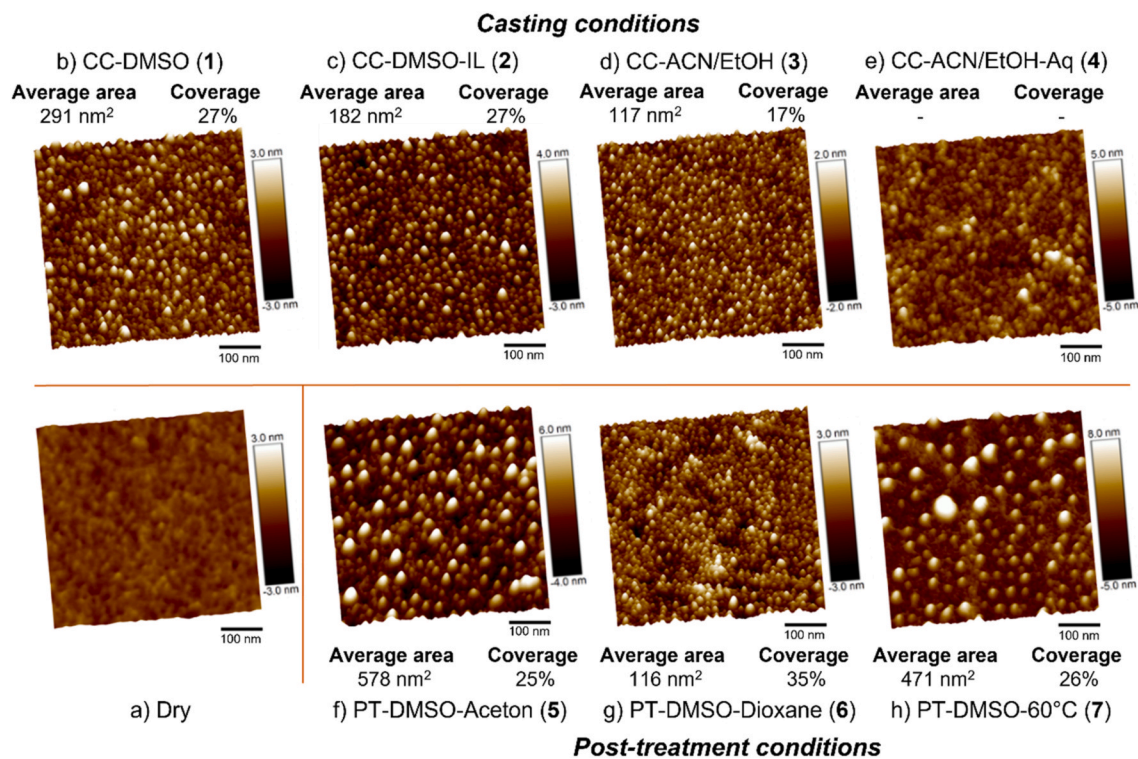


Fig. 1. 3D-Topographic AFM images of all fabricated membranes after water uptake (b–h) and exemplary of CC-DMSO (1) in dry state (a). Images were taken by the PeakForce Tapping® method to obtain the topography with a resolution of 500 nm × 500 nm. Average area of hydrophilic domains and surface coverage by these domains were analyzed via image analysis (see Section 2.2 and SI).

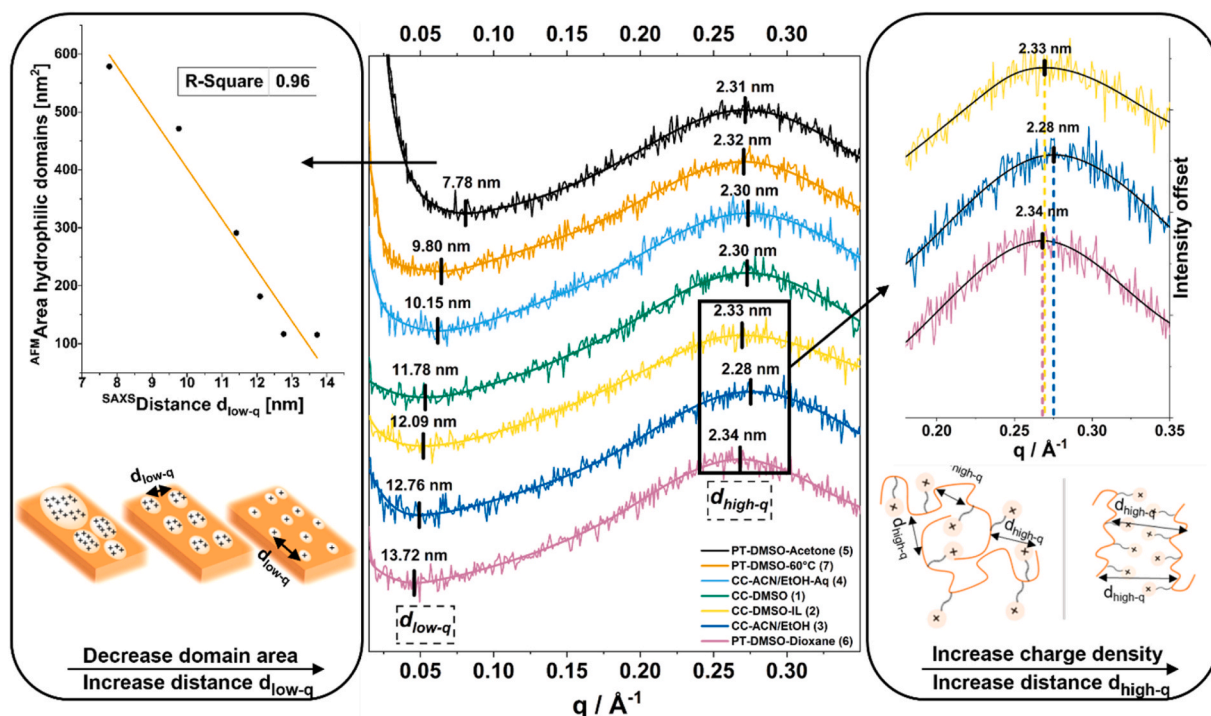


Fig. 2. Results of SAXS measurements detecting scattering vectors between 0.02 and 0.35 Å. (Middle) SAXS raw data plots underlined with the interpolated curves for all membranes with intensity offset for comparison; determined peaks are marked with the corresponding Bragg's distance d (cf. Eq. (2)). (Left) Comparison of d_{low-q} at small scattering vectors with the hydrophilic domain areas of the corresponding membranes from AFM and schematic depiction of d_{low-q} between hydrophilic domains. (Right) Comparison of the large scattering vector d_{high-q} peak for membranes 2, 3 and 6 and schematic depiction of d_{high-q} distances between polymer backbones in the hydrophilic domains.

Table 3

Measured dry density, water uptake and thickness swelling for all fabricated membranes.

Membrane	Dry density [mg/mm ³]	Water uptake [%]	Swelling [%]
CC-DMSO (1)	1.39	14.4	4.1
CC-DMSO-IL (2)	1.35	28.7	4.5
CC-ACN/EtOH (3)	1.25	14.5	5.1
CC-ACN/EtOH-Aq (4)	1.22	14.7	5.2
PT-DMSO-Acetone (5)	1.29	17.3	4.2
PT-DMSO-Dioxane (6)	1.44	25.0	11.8
PT-DMSO-60 °C (7)	1.29	13.6	1.4

high- q region corresponds to small distances in single clusters and that the minimum peak in the low- q region corresponds to distances between different clusters [48].

For the low- q distance (d_{low-q}) we observed significant differences for all fabrication conditions with values between 7.78 nm and 13.72 nm (Fig. 2, middle). We also found that a larger low- q distance directly correlates to a smaller hydrophilic domain area measured via AFM as shown by a good linear fit ($R^2 = 0.96$, Fig. 2, left). This is reasonable because enlarged domains should result in closer contact to each other. On the other hand, this contrasts the AFM images shown in Fig. 1 where a closer contact between smaller regions can be observed. This can be explained with the water uptake and subsequent swelling of hydrophilic domains in the membranes analyzed in the AFM measurements (Fig. 1) and the fact that SAXS was measured with dry membranes. Additionally, SAXS depicts the morphology of the whole membrane which could mean that the overall density of hydrophilic domains is lower in the membrane than on the surface. Overall, the d_{low-q} values verify the size trends observed via AFM and support the above discussed influences of the

fabrication conditions. With SAXS we now also found that the addition of water for membrane 4 did lead to an increase in domain sizes as shown by the low d_{low-q} of 10.15 nm, likely because of a better mobility of hydrophilic domains.

The high- q region distances d_{high-q} are rather similar for all membranes, with CC-ACN/EtOH (3) having the smallest value of 2.28 nm (Fig. 2, middle). This value was slightly increased when using DMSO as casting solvent (Membrane 1, 2.30 nm) or water as additive (Membrane 4, 2.30 nm) as well as after annealing with acetone (Membrane 5, 2.31 nm) or at 60 °C (Membrane 7, 2.32 nm). The most significant changes were achieved for the membranes CC-DMSO-IL (2) and PT-DMSO-Dioxane (6) with 2.33 nm and 2.34 nm, respectively (Fig. 2, right). While the observed differences are small, the used SAXS method results in an error of ± 0.006 nm for these values which still allows us to make statements about the general trend of d_{high-q} . Konishi et al. [48] showed that the d_{high-q} values correspond to distances in single clusters, and accordingly we assigned d_{high-q} to the distances between different polymer backbones in an individual hydrophilic domain. Based on our data we propose that the observed hydrophilic regions with sizes of up to several 10s of nanometers consist of multiple macromolecules and include both backbone and charged side chains. The phase segregation could then be a result of unfolding of polymer coil structures to present the side chain groups, which results in more accessible charges and also an increased distance between different backbones (Fig. 2, right). The smaller d_{high-q} of the fast dried membrane 3 can then be attributed to a solidification while the different polymer backbones in the domains are still partially entangled. For the other membranes this disentanglement process was completed, resulting in similar d_{high-q} . Furthermore, we think that for membrane 2 the ionic liquid enabled better clustering of charged groups and subsequently led to a backbone orientation away from the charge center which results in the larger d_{high-q} distance. The post-treatment with 1,4-dioxane (6) led to solvent uptake into the hydrophobic bulk. This could have attracted the hydrophobic backbones in

the charged regions at the boundary with the bulk matrix which then directed the charged groups inwards and increased the d_{high-q} distance. The resulting higher local charge accessibility in both membranes **2** and **6** is also indicated in the AFM measurements by a higher local water uptake and subsequently more pronounced elevation of hydrophilic regions in comparison to membranes with similar domain size (**2** vs. **1**, **6** vs. **3**; cf. Fig. 1).

Overall, these observations imply that we can use larger d_{high-q} values as an indicator for a better accessibility of side chains and consequently higher local charge density in the hydrophilic domains. However, that we did observe values in the same range for the different fabrication conditions means that the hydrophilic regions do not enlarge by a growing distance between charged side chains. This supports again that the enlargement is more likely a result of an assembly of different contacting regions.

3.3. Macroscopic structural properties

Besides changes in nanoscale morphology, the fabrication conditions also led to membranes with significant differences in their macroscopic structural properties (Table 3).

For all membranes the same ion-exchange capacity (IEC) of around 0.8 mmol/g was measured, which shows that the observed changes in local charge accessibility did not directly impact the overall accessibility of charged groups (see Table S2 in SI). However, this could also be due to the long incubation of membranes in the solutions used for IEC determination which may result in the measurement of charged groups not located in the hydrophilic domains (see Section S6 in SI). While both hydrophobic and hydrophilic parts of the membrane contribute to the density, the overall larger hydrophobic portion means that the membrane density is a good indicator for the free volume in the amorphous matrix (Table 3). The membranes made from DMSO show a dry density of 1.39 mg/mm³ (**1**), respectively 1.35 mg/mm³ (**2**). This is significantly higher than what we observed when using the fast evaporating ACN/EtOH mixture, which resulted in densities of 1.25 mg/mm³ (**3**) and 1.22 mg/mm³ (**4**). These changes suggest that the hydrophobic parts are also in the non-equilibrium state and move over time towards a reduced free volume. The density of membrane **1** was further increased to 1.44 mg/mm³ by treatment with 1,4-dioxane (**6**), proving that 1,4-dioxane successfully solvated the hydrophobic regions and changed the free volume in the amorphous matrix over time. On the other hand, the addition of ionic liquid to DMSO (**2**) led to a lower dry density of 1.35 mg/mm³ in comparison to membrane **1** that was made without the additive. The ionic liquid can likely occupy the space between polymer chains which subsequently inhibits a free volume reduction. The decrease in density by treatment with polar acetone (**5**) to 1.29 mg/mm³ can be attributed to the enlargement of hydrophilic domains. The treatment at 60 °C (**7**) resulted in the same density and also similar hydrophilic domains (Fig. 1) as the annealing with acetone (**5**), which means that an elevated temperature only increased the mobility in the hydrophilic regions and not in the hydrophobic bulk.

All membranes show a water uptake of around 15%, with the only exceptions being CC-DMSO-IL (**2**) (28.7%) and PT-DMSO-Dioxane (**6**) (25.0%). Both these membranes also showed a higher local water uptake in the AFM measurements and the SAXS data suggests more accessible charged groups in the hydrophilic domains than for the rest of the membranes. On the other hand, this correlation to the macroscopic water uptake was not observed for the other membranes and in general the water uptake cannot be directly attributed to a single structural component. Several studies already established that a high water uptake is an indicator for the formation of long-range void spaces that form water pathways through the membrane. These water pathways are not necessarily identical to the hydrophilic domains but are also influenced by the overall polymer packing, material flexibility and backbone polarity [49–51]. This means that the fabrication conditions for **2** and **6** resulted in materials with properties that are in sum beneficial for water

uptake. Surprisingly, for CC-DMSO-IL (**2**) the higher water uptake was not accompanied with a higher thickness swelling, which could be due to the ionic liquid inhibiting a reduction in free volume during fabrication which then enables uptake of water volume without swelling. This result is especially interesting because increasing the water uptake of AEMs while maintaining mechanical integrity is notoriously difficult to achieve but necessary to overcome the current limitations of AEMs.

In summary, we can postulate a model for the nanophase segregation mechanism that could be responsible for the final membrane morphology (Fig. 3).

First, during the evaporation of the casting solvent, a spontaneous division into small clusters with more charged side chains occurs. After this initial segregation, the different macromolecules in these hydrophilic clusters are still partially entangled. Over time they move towards higher ordering which is characterized by an increase in distance between different backbones. This results in a favorable presentation of the charged side chains and higher local charge density. This process can be inhibited by using a fast evaporating solvent while both the addition of ionic liquid and annealing with 1,4-dioxane increased the effectivity of this process. The hydrophilic domains formed by disentanglement then enlarge in a second step, which is driven by the repulsion between the positively charged side chains. The domains move towards equilibrium state over time and the size increase is facilitated by incorporation of new macromolecular segments and neighboring domains. This results in only small changes in both the surface coverage and the distance between the different macromolecules. This enlargement was increased by conditions that lead to a longer mobility in the hydrophilic domains, namely a slower evaporating solvent and annealing with acetone or at 60 °C. On the other hand, in the hydrophobic bulk the equilibrium is reached by a decrease of free volume in the amorphous matrix. This was facilitated by a slower drying solvent and by annealing with the non-polar solvent 1,4-dioxane. In contrast, by adding an ionic liquid to the casting solution the reduction in free volume was partially inhibited.

In summary, the nanoscale morphology can be rationally tuned to tailor specific membrane properties like hydrophilic domain size, local charge density, water uptake or long range-ordering. With these new insights we can also give a more in-depth explanation for results of other published works. For example, we can now attribute the observation that non-polar casting solvents lead to small hydrophilic domains to the hindered mobility in these regions and subsequent solidification in the non-equilibrium state [28]. Furthermore, we can give an alternative explanation for results of works that describe the membrane nanostructure solely to be affected by the polarity of the used solvents, although membranes were fabricated at the same drying temperature with solvents with significantly different vapor pressure [52].

3.4. Acid diffusion rates

To investigate the influence of the membrane nanostructure on the acid transport performance, we conducted diffusion dialysis experiments for all fabricated membranes with HBr, HCl and acetic acid in the feed solution and measured the acid concentration via the pH of the permeate over time. For all membranes a linear increase of permeate concentration over 30 min was observed, and from the flux and the initial acid concentration (1 M) the effective diffusion coefficients were calculated using Fick's first law (see Fig. S12 in SI); results are shown in Fig. 4.

Comparing how the different fabrication conditions changed the diffusion shows that an increase in HBr diffusion rate was accompanied by the same increase in HCl diffusion rate. This means that in all membranes the two inorganic acids are transported by the same pathway. The generally lower effective diffusion coefficients for HCl than for HBr are likely due to the larger hydrodynamic radius of Cl⁻ [53]. On the other hand, we found that the membranes depict different relationships between the HBr and acetic acid diffusion as shown by the theoretical selectivity (Fig. 4, bottom). This means that the inorganic

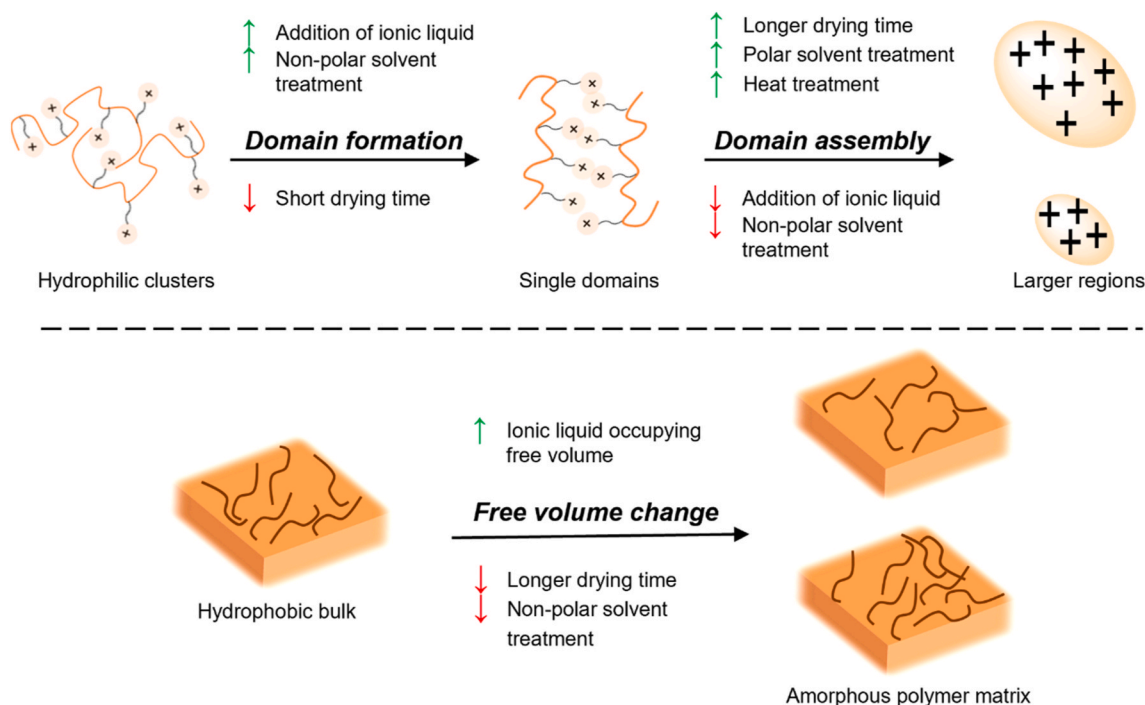
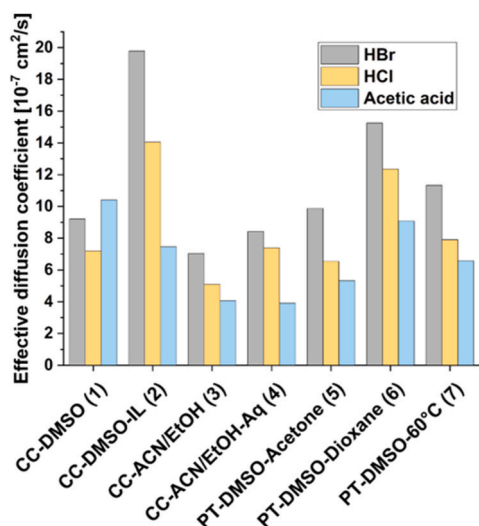


Fig. 3. Proposed mechanism for the formation of a nanophase segregated morphology influenced by the fabrication conditions and resulting in different membrane nanostructures.



	D [10^{-7} cm ² /s]			Selectivity ^a
	HBr	HCl	Acetic acid	
CC-DMSO (1)	9.2	7.2	10.4	0.9
CC-DMSO-IL (2)	19.8	14.0	7.5	2.7
CC-ACN/EtOH (3)	7.0	5.1	4.1	1.7
CC-ACN/EtOH-Aq (4)	8.4	7.4	3.9	2.2
PT-DMSO-Acetone (5)	9.9	6.5	5.3	1.9
PT-DMSO-Dioxane (6)	15.3	12.4	9.1	1.7
PT-DMSO-60°C (7)	11.3	7.9	6.6	1.7

Fig. 4. (Top) Effective diffusion coefficients for all membranes for HBr, HCl and acetic acid shown as a bar graph for visual comparison. (Bottom) Values for the effective diffusion coefficients for all membranes for HBr, HCl and acetic acid and HBr/Acetic acid selectivity calculated from the single solute data.^a

acid and acetic acid transport processes are influenced by different membrane properties and that the different properties were individually altered by the fabrication conditions. For the HBr diffusion dialysis the membrane made with ionic liquid additive (2) led to the highest apparent diffusion coefficient of 19.8×10^{-7} cm²/s. All three membranes that were annealed in the post-treatment also show an increased transport rate compared to the precursor membrane 1, while the fast evaporating solvent yielded the membranes (3, 4) with the lowest apparent diffusion coefficients. In regard to the corresponding membrane morphologies we found a linear correlation of the HBr diffusion coefficients to parameters of the hydrophilic domain structure, namely to the d_{high-q} distance ($R^2 = 0.96$) and to the surface coverage with hydrophilic domains ($R^2 = 0.88$) as shown in Fig. 5.

We discussed above (Fig. 2) that the d_{high-q} distance relates to distances between different macromolecular segments in the hydrophilic domains and that this value can be used to describe the presentation of the charged side chains. This means that the positive influence of a larger d_{high-q} distance indicates that a higher charge accessibility is beneficial for HBr diffusion and that the inner structure of hydrophilic domains is mostly responsible for the HBr transport. Furthermore, the increased transport rates for membranes with a higher surface coverage by hydrophilic domains means that the inorganic acids are foremost taken up into the membrane and subsequently transported to the other side by the individual hydrophilic domains. Together this shows that the hydrophilic domains likely act as charged nanochannels and that diffusion is directly facilitated by the charged polymer groups. That we found a significantly higher diffusion coefficient for CC-DMSO-IL (2) that does not fit to these linear correlations suggests that the addition of ionic liquid led to further positive changes in the membrane structure that were not detected by AFM or SAXS. The ionic liquid addition is also the only condition that contributed actively to the membrane structuring and did not only influence the mobility of chain segments or the duration until solidification.

For the diffusion of acetic acid, membrane CC-DMSO (1) surprisingly achieved the highest diffusion coefficient (10.4×10^{-7} cm²/s), while showing one of the lowest diffusion rates for Br⁻ and Cl⁻. The annealing with 1,4-dioxane led to a slight decrease of the diffusion coefficient to

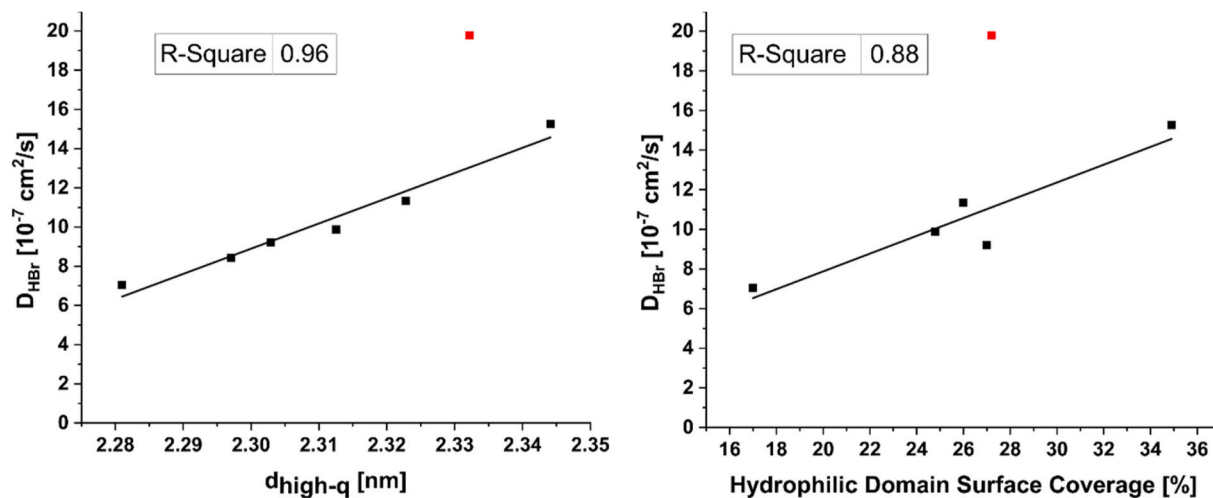


Fig. 5. Distance $d_{\text{high-q}}$ (SAXS, Fig. 2) and hydrophilic domain surface coverage (AFM, Fig. 1) in relation to the effective diffusion coefficients of HBr that were measured for the respective membranes. Data points for the membrane made with ionic liquid additive (2) were excluded for the linear fit (in red). (For interpretation of the references to colour in this figure legend, the reader is referred to the Web version of this article.)

$9.1 \cdot 10^{-7} \text{ cm}^2/\text{s}$, while the addition of ionic liquid and post-treatment with acetone and at $60 \text{ }^\circ\text{C}$ led to significantly lower transport rates. For acetic acid, the use of the fast evaporating solvent (3, 4) led again to the membranes with the worst transport performance. With the exception of PT-DMSO-Dioxane (6), all fabrication conditions that led to a decrease in acetic acid diffusion rate also led to a lower membrane density. For this relationship we could again find a good linear correlation with a R^2 value of 0.88 (Fig. 6).

The dry density is mostly a result of the hydrophobic bulk which means that the bulk nanostructure has a direct influence on the acetic acid transport. This influence suggests that acetic acid diffuses through the hydrophobic parts of the membrane. That the diffusion is faster for more dense membranes with less free volume could be explained by the higher ordering and subsequently a formation of long-range connected void spaces that act as hydrophobic nanopores (as also indicated in the nanophase segregation model in Fig. 3). Li et al. similarly observed that a higher ordered graphene oxide membrane led to less constricted nanopores and higher water permeance [54]. That the transport via these hydrophobic nanopores is only observed for acetic acid could be

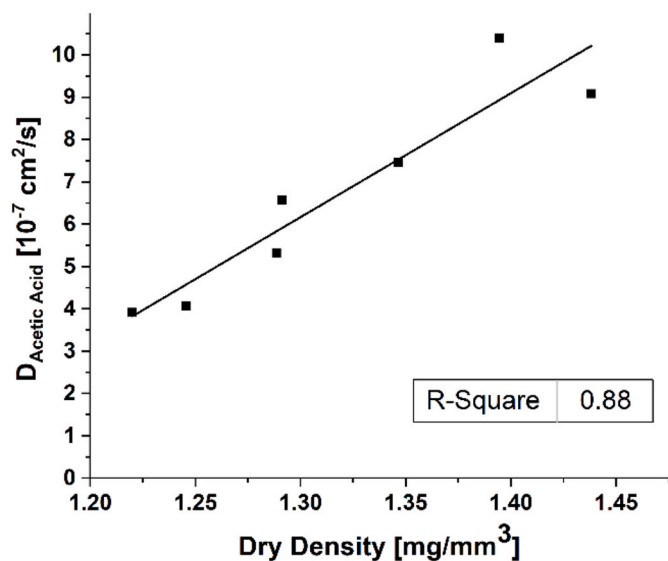


Fig. 6. Dry density in relation to the effective diffusion coefficients for acetic acid that were measured for the respective membranes.

due to the low solvation energy of non-dissociated acetic acid in comparison to Br^- and Cl^- and additionally due to the pK_a of 4.76 that results in a low concentration of acetate anions (>99% protonated acetic acid under the experimental conditions) [55]. This is also supported by recent research into the transport mechanisms in nanofiltration membranes that found ion dehydration to be the main membrane entry barrier [56,57]. That this physical pathway exists for the acetic acid transport would also explain why the fabrication conditions independently changed the transport rates for the inorganic acids and acetic acid.

To further investigate the above proposed transport mechanisms we conducted solute mixture diffusion dialysis tests for membrane CC-DMSO (1) (Fig. 7).

We used combinations of acetic acid, HBr and salts in the feed solution and measured the concentrations in the permeate after 30 min of dialysis via ion chromatography (IC). The measurement via IC yielded the same transport rates for the single acids as the pH method used for the above discussed experiments (Fig. 7b, right). To exclude the effects of different initial counter-ion and acid concentrations in the membrane, we conditioned the membranes for 30 min in the respective feed composition before each measurement.

In contrast to the single acid measurements for membrane 1, a significantly higher flux for HBr than for acetic acid was observed for the combination of 1 M acetic acid with 1 M HBr (Fig. 7a). As expected, the flux for both species decreased at lower concentrations but surprisingly for Br^- it converged towards the flux of acetic acid, with equal values at a feed concentration of 0.1 M for each species. Normalizing the flux to the concentration difference as driving force reveals that acetic acid has the same diffusion rate in all combinations with HBr (Fig. 7b, left). This means that the acetic acid diffusion was independent on the amount of HBr transported through the membrane. We further observed the same diffusion rate for acetic acid in the single acid experiments as in presence of HBr (Fig. 7b, right). This underlines that two independent physical pathways exist in these membranes that lead to a simultaneous transport of both HBr and acetic acid. It also shows that acetic acid is not transported in the deprotonated form because the diffusion behavior did not change at low pH (through HBr addition). We further did not see a decreased acetic acid transport rate in presence of 0.1 M NaBr or 0.1 M KCl but did observe both Br^- and Cl^- diffusion through the membrane. This means that the halide anions can be transported together with protons from the acetic acid while acetic acid itself is transported without charge (we did not observe any cation crossover).

For the Br^- transport rate we saw a 2.5-fold increase when combined

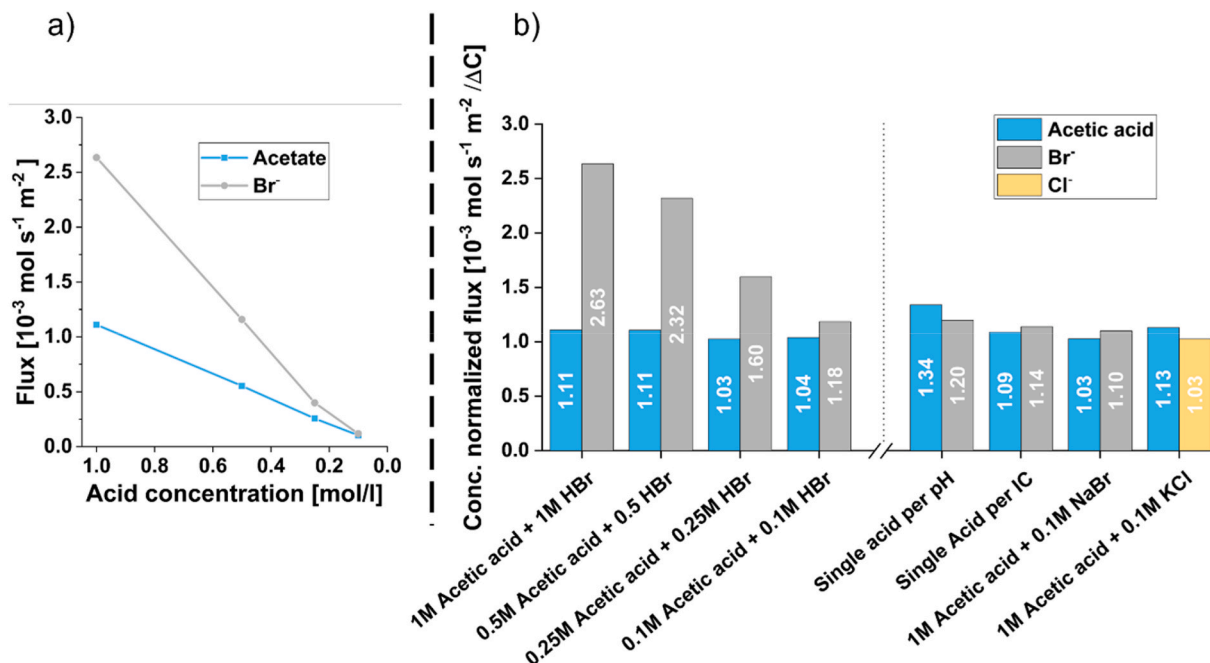


Fig. 7. Results of the mixed acid diffusion dialysis for membrane CC-DMSO (1). a) Acid flux in relation to the concentration of each acid. b) Concentration normalized flux of each acid for the different conditions in the feed chamber.

with acetic acid at 1 M concentration. The reason for this could be that the overall high concentration positively influenced the membrane structure for Br^- diffusion. That this behavior is not observed for acetic acid is again a proof for different transport mechanisms. It is also in line with the morphology of the proposed respective pathways because the hydrophobic nanopores are likely not in direct contact with the feed solution while the feed should be able to partially enter and alter the charged domains. Overall, we found that every single fabrication condition had an influence on the acid transport and that our developed conditions led to particular membranes with significantly increased effective diffusion coefficients.

3.5. Ionic conductivity

For the measurement of the ionic conductivity of AEMs, an in-plane 4-probe set up is routinely used in which the electrodes are directly placed onto the membrane without the use of any electrolyte. However, it was already shown that the through-plane and in-plane ionic conductivities significantly differ for most membranes [58]. Furthermore, the in-plane conductivity gives only little insights into the influence of the nanostructure on transport through the membrane. Here, we used a homemade conductivity cell to measure the through-plane conductivity in KOH at 20 °C (see Section 2.3 and Fig. S10 in SI) and the obtained specific ionic conductivities are shown in Fig. 8. It has to be mentioned that the conductivities obtained with this method are inherently lower than for the routinely used in-plane 4-probe set ups. This is due to the low temperature we used and also due to the full immersion in electrolyte which leads to a lower membrane hydration and subsequently higher ionic resistance [59].

Membranes CC-DMSO-IL (2) and PT-DMSO-Dioxane (6) show the best transport properties, with OH^- conductivities of 9.4 mS/cm and 15.5 mS/cm. The ionic conductivities for all other membranes lie between 3 and 5 mS/cm which can be considered as non-significant differences when including the standard deviation. This shows that the OH^- transport in the membranes does not directly relate to the corresponding HBr diffusion rates (Fig. 4). Also, the overall performance discrepancy is significantly larger than for the acid diffusion, with a more than 5-fold increase in conductivity for membrane 6 compared to membrane 4. In

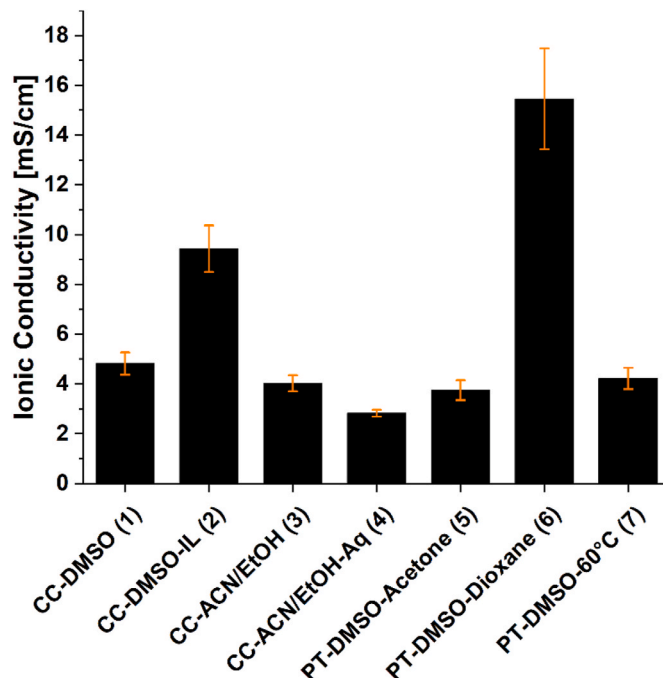


Fig. 8. Through-plane ionic conductivity for all membranes measured in 1 M KOH at 20 °C with the standard deviation shown in orange. (For interpretation of the references to colour in this figure legend, the reader is referred to the Web version of this article.)

general, the different ionic conductivities can be connected to the differences in water uptake (Table 3), with membranes 2 and 6 showing a larger uptake of 28.7% and 25.0% while the rest of the membranes show values between 13.6% and 17.3%. The annealing with 1,4-dioxane (6) did also lead to an increased swelling after water uptake, which can result in a more connected water network in the membrane and explains the best OH^- transport performance. This means that the ionic conductivity can be ascribed to a transport by water pathways in the interstitial

phase. While the hydrophilic domains, or charged nanochannels, are part of this phase it further consists of non-charged but hydrophilic void spaces that can take up water and the water filled void spaces that are formed by membrane swelling. In the interstitial phase the normal diffusion processes take place and the charged polymer groups do not actively facilitate a transport. That we only observed this transport behavior for the ionic conductivity and not the inorganic acid diffusion can be explained with the Grotthuss mechanism. OH^- can accept a proton from a nearby water molecule, generating a new hydroxide species, which again is protonated by the next water molecule resulting in fast diffusion without direct movement. Overall, we found a third transport pathway for the ionic conductivity that is not directly influenced by the nanostructure but by the macroscopic water uptake and the subsequent membrane swelling.

3.6. Combined transport model

From the above results we can form a combined transport model consisting of three mechanisms which all correspond to different structural pathways: a water filled interstitial phase, charged nanochannels and hydrophobic nanopores (Fig. 9).

The conductivity of OH^- seems to be based on the transport along the water pathways of the interstitial phase. The diffusion rate for OH^- increases in water through the Grotthuss mechanism which makes a facilitated transport by the polymer groups in the charged nanochannels unfavourable. Both the overall bound water volume and connectivity of water pathways were found to be beneficial for a higher ionic conductivity. For HBr and HCl our data suggests a hopping of anions between charged side chains in the nanochannels which likely increases the drag across the membrane and favours this mechanism relative to a normal diffusion through the water filled interstitial phase. Furthermore, the high solvation energy of anions inhibits the entry into the hydrophobic nanopores. The main membrane properties contributing to the transport via charged nanochannels were found to be an increased ordering in the

hydrophilic domains, a high local charge density and a high surface coverage with hydrophilic regions. For acetic acid we found a possible transport by hydrophobic nanopores. A low solvation energy enables pore entry and the interaction with the hydrophobic pore walls could facilitate movement along the concentration gradient that is favoured relative to diffusion via water pathways. The low concentration of the charged acetic acid form also limits an effective transport via charged nanochannels. The hydrophobic nanopores are mainly influenced by the ordering in the amorphous hydrophobic bulk, with ordering over a longer time likely resulting in the formation of connected void spaces through the membrane which increases the transport rate. As shown during the discussion of the fabrication conditions, all these different membrane properties can be tuned by the methods employed in this work and even selectively targeted to independently control the structure of the different pathways. In this study we found no direct influence of the average size of hydrophilic domains on transport rates, which shows that most likely the other here presented factors overshadow the influence of this parameter. This is also in line with examples found in literature that show a positive effect of small nanochannels on the ionic conductance in some cation-exchange membranes, while other authors observed an increase in conductivity for larger hydrophilic domain sizes [60,61].

4. Conclusions

Our results clearly demonstrate that we successfully employed several fabrication conditions to adjust the nanoscale morphology of anion-exchange membranes made from the same polymer, and that this morphology significantly influences the exhibited ion transport rates. We were able to elucidate the processes during self-assembly of the used charged polymer into ordered hydrophilic domains and hydrophobic bulk matrix. We concluded that hydrophilic domains are shaped after the nanophase segregation by a disentanglement of different polymer chains that increases the overall accessibility of charged groups. In a

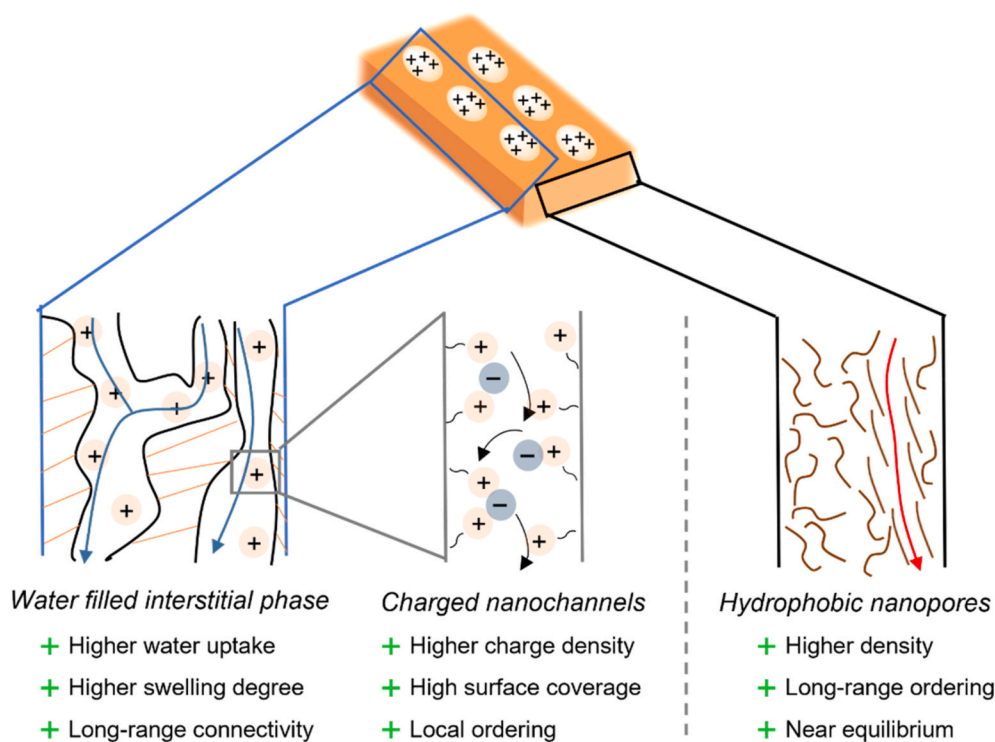


Fig. 9. The proposed transport model that consists of three different structural pathways that all coexist in each membrane. Green pluses show the membrane properties that increase the transport rate via the respective pathway. (For interpretation of the references to colour in this figure legend, the reader is referred to the Web version of this article.)

second step, initiated by charge repulsion, these regions grow in size by incorporating neighboring domains. On the other hand, the hydrophobic bulk matrix moves towards higher ordering and less free volume over time. We were able to independently control both mechanisms, by utilizing different drying times during the membrane fabrication, by employing a solvent post-treatment that selectively increases the movement of only one of the nanophases and by compensating the repulsion between charged side chains through the addition of an ionic liquid. We could also show that Br⁻/Cl⁻, acetic acid and OH⁻ are all transported through different mechanisms and could relate these to the membrane structure. Besides new insights into the fundamental transport processes in AEMs, we were able to significantly improve the performance of the membranes, achieving a 5-fold increase in ionic conductivity and 3-fold increase in acid diffusion rate while simultaneously altering the selectivity towards the different acids. Overall, this study shows methods to tailor the properties of anion-exchange membranes through their fabrication conditions resulting in an optimized performance. This could enable a more rational membrane development approach for important applications in the fields of energy technologies, waste recycling or water treatment.

Credit author statement

Lukas Fischer: Conceptualization, Methodology, Investigation, Formal analysis, Data curation, Writing – original draft; **Sven Sören Hartmann:** Investigation; **Artjom Maljusch:** Writing – review & editing, Project administration; **Christian Däschlein:** Writing – review & editing, Project administration; **Oleg Prymak:** Investigation, Formal analysis, Writing – review & editing; **Mathias Ulbricht:** Conceptualization, Methodology, Supervision, Funding acquisition.

Declaration of competing interest

The authors declare that they have no known competing financial interests or personal relationships that could have appeared to influence the work reported in this paper.

Data availability

Data will be made available on request.

Acknowledgements

This work has been performed in the frame of the INNOMEM project that has received funding from the European Union's Horizon 2020 Research and Innovation Program under Grant Agreement N° 862330. We would like to thank Dr. Steffen Franzka from the Interdisciplinary Center for Analytics on the Nanoscale (ICAN) at University Duisburg-Essen (UDE) for conducting the AFM measurements as well as the UDE students Natalie Wolff, Niklas Cendrowski, Simon Mennicken and Christian Rex for assisting with laboratory work. We also thank Dr. Falko Mählendorf and Dr. David Fuchs from the Chair of Energy Technology, UDE, for allowing us to use their equipment for the ionic conductivity measurements.

Appendix A. Supplementary data

Supplementary data to this article can be found online at <https://doi.org/10.1016/j.memsci.2022.121306>.

References

- [1] J.R. Varcoe, P. Atanassov, D.R. Dekel, A.M. Herring, M.A. Hickner, P.A. Kohl, A. R. Kucernak, W.E. Mustain, K. Nijmeijer, K. Scott, T.W. Xu, L. Zhuang, Anion-exchange membranes in electrochemical energy systems, *Energy Environ. Sci.* 7 (2014) 3135–3191, <https://doi.org/10.1039/c4ee01303d>.
- [2] C. Zhang, W. Zhang, Y. Wang, Diffusion dialysis for acid recovery from acidic waste solutions: anion exchange membranes and Technology integration, *Membranes* 10 (2020) 169, <https://doi.org/10.3390/membranes10080169>.
- [3] S.P. Nunes, P.Z. Culfaz-Emecen, G.Z. Ramon, T. Visser, G.H. Koops, W.Q. Jin, M. Ulbricht, Thinking the future of membranes: perspectives for advanced and new membrane materials and manufacturing processes, *J. Membr. Sci.* 598 (2020), 117761, <https://doi.org/10.1016/j.memsci.2019.117761>.
- [4] R.S. El-Emam, H. Ozcan, Comprehensive review on the techno-economics of sustainable large-scale clean hydrogen production, *J. Clean. Prod.* 220 (2019) 593–609, <https://doi.org/10.1016/j.jclepro.2019.01.309>.
- [5] H.A. Miller, K. Bouzek, J. Hnat, S. Loos, C.I. Bernaeker, T. Weissgarber, L. Rontzsch, J. Meier-Haack, Green hydrogen from anion exchange membrane water electrolysis: a review of recent developments in critical materials and operating conditions, *Sustain. Energy Fuels* 4 (2020) 2114–2133, <https://doi.org/10.1039/c9se01240k>.
- [6] J.Y. Luo, C.M. Wu, T.W. Xu, Y.H. Wu, Diffusion dialysis-concept, principle and applications, *J. Membr. Sci.* 366 (2011) 1–16, <https://doi.org/10.1016/j.memsci.2010.10.028>.
- [7] M. Regel-Rosocka, A review on methods of regeneration of spent pickling solutions from steel processing, *J. Hazard Mater.* 177 (2010) 57–69, <https://doi.org/10.1016/j.jhazmat.2009.12.043>.
- [8] S. Jiang, H. Sun, H. Wang, B.P. Ladewig, Z. Yao, A comprehensive review on the synthesis and applications of ion exchange membranes, *Chemosphere* 282 (2021), 130817, <https://doi.org/10.1016/j.chemosphere.2021.130817>.
- [9] G. Merle, M. Wessling, K. Nijmeijer, Anion exchange membranes for alkaline fuel cells: a review, *J. Membr. Sci.* 377 (2011) 1–35, <https://doi.org/10.1016/j.memsci.2011.04.043>.
- [10] L. Wang, F. Zhang, Z.X. Li, J.Y. Liao, Y.D. Huang, Y.L. Lei, N.W. Li, Mixed-charge poly(2,6-dimethyl-phenylene oxide)anion exchange membrane for diffusion dialysis in acid recovery, *J. Membr. Sci.* 549 (2018) 543–549, <https://doi.org/10.1016/j.memsci.2017.12.054>.
- [11] K. Emmanuel, C.L. Cheng, B. Erigene, A.N. Mondal, M.M. Hossain, M.I. Khan, N. Ul Afsar, G. Liang, L. Wu, T.W. Xu, Imidazolium functionalized anion exchange membrane blended with PVA for acid recovery via diffusion dialysis process, *J. Membr. Sci.* 497 (2016) 209–215, <https://doi.org/10.1016/j.memsci.2015.09.043>.
- [12] A.N. Mondal, C. Cheng, M.I. Khan, M.M. Hossain, K. Emmanuel, L. Ge, B. Wu, Y. He, J. Ran, X. Ge, Improved acid recovery performance by novel Poly (DMAEM-co-y-MPS) anion exchange membrane via diffusion dialysis, *J. Membr. Sci.* 525 (2017) 163–174, <https://doi.org/10.1016/j.memsci.2016.10.042>.
- [13] M. Tanaka, K. Fukasawa, E. Nishino, S. Yamaguchi, K. Yamada, H. Tanaka, B. Bae, K. Miyatake, M. Watanabe, Anion conductive block poly(arylene ether)s: synthesis, properties, and application in alkaline fuel cells, *J. Am. Chem. Soc.* 133 (2011) 10646–10654, <https://doi.org/10.1021/ja204166e>.
- [14] G.G. Wang, Y.M. Weng, D. Chu, R.R. Chen, D. Xie, Developing a polysulfone-based alkaline anion exchange membrane for improved ionic conductivity, *J. Membr. Sci.* 332 (2009) 63–68, <https://doi.org/10.1016/j.memsci.2009.01.038>.
- [15] W.H. Lee, E.J. Park, J. Han, D.W. Shin, Y.S. Kim, C. Bae, Poly(terphenylene) anion exchange membranes: the effect of backbone structure on morphology and membrane property, *ACS Macro Lett.* 6 (2017) 566–570, <https://doi.org/10.1021/acsmacrolett.7b00148>.
- [16] M. Kumari, J.C. Douglas, D.R. Dekel, Crosslinked quaternary phosphonium-functionalized poly(ether ether ketone) polymer-based anion-exchange membranes, *J. Membr. Sci.* 626 (2021), 119167, <https://doi.org/10.1016/j.memsci.2021.119167>.
- [17] G. He, Z. Li, J. Zhao, S. Wang, H. Wu, M.D. Guiver, Z. Jiang, Nanostructured ion-exchange membranes for fuel cells: recent advances and perspectives, *Adv. Mater.* 27 (2015) 5280–5295, <https://doi.org/10.1002/adma.201501406>.
- [18] J. Kamcev, D.R. Paul, G.S. Manning, B.D. Freeman, Ion diffusion coefficients in ion exchange membranes: significance of counterion condensation, *Macromolecules* 51 (2018) 5519–5529, <https://doi.org/10.1021/acs.macromol.8b00645>.
- [19] N.U. Afsar, B. Erigene, M. Irfan, B. Wu, T. Xu, W. Ji, K. Emmanuel, L. Ge, T.J. Xu, High performance anion exchange membrane with proton transport pathways for diffusion dialysis, *Separ. Purif. Technol.* 193 (2018) 11–20, <https://doi.org/10.1016/j.seppur.2017.10.062h>.
- [20] Y. Zhao, K. Yoshimura, H. Takamatsu, A. Hiroki, Y. Kishiyama, H. Shishitani, S. Yamaguchi, H. Tanaka, S. Koizumi, A. Radulescu, M.S. Appavou, Y. Maekawa, Imidazolium-based anion exchange membranes for alkaline anion fuel cells: interplay between morphology and anion transport behavior, *J. Electrochem. Soc.* 166 (2019) F472–F478, <https://doi.org/10.1149/2.0431908jes>.
- [21] Q. Gui, Q. Ouyang, C. Xu, H. Ding, S. Shi, X. Chen, Facile and safe synthesis of novel self-pored amine-functionalized polystyrene with nanoscale bicontinuous morphology, *Int. J. Mol. Sci.* 21 (2020) 9404, <https://doi.org/10.3390/ijms21249404>.
- [22] A.N. Lai, L.S. Wang, C.X. Lin, Y.Z. Zhuo, Q.G. Zhang, A.M. Zhu, Q.L. Liu, Phenolphthalein-based poly(arylene ether sulfone nitrile)s multiblock copolymers as anion exchange membranes for alkaline fuel cells, *ACS Appl. Mater. Interfaces* 7 (2015) 8284–8292, <https://doi.org/10.1021/acsami.5b01475>.
- [23] T. Huang, G.W. He, J.D. Xue, O. Otoo, X.Y. He, H.F. Jiang, J.F. Zhang, Y. Yin, Z. Y. Jiang, J.C. Douglas, D.R. Dekel, M.D. Guiver, Self-crosslinked blend alkaline anion exchange membranes with bi-continuous phase separated morphology to enhance ion conductivity, *J. Membr. Sci.* 597 (2020), 117769, <https://doi.org/10.1016/j.memsci.2019.117769>.
- [24] J. Wiecezorek, M. Ulbricht, Amphiphilic poly(arylene ether sulfone) multiblock copolymers with quaternary ammonium groups for novel thin-film composite

- nanofiltration membranes, *Polymer* 217 (2021), 123446, <https://doi.org/10.1016/j.polymer.2021.123446>.
- [25] Y.B. He, J.J. Si, L. Wu, S.L. Chen, Y. Zhu, J.F. Pan, X.L. Ge, Z.J. Yang, T.W. Xu, Dual-cation comb-shaped anion exchange membranes: structure, morphology and properties, *J. Membr. Sci.* 515 (2016) 189–195, <https://doi.org/10.1016/j.memsci.2016.05.058>.
- [26] R. Guan, H. Dai, C.H. Li, J.H. Liu, J. Xu, Effect of casting solvent on the morphology and performance of sulfonated polyethersulfone membranes, *J. Membr. Sci.* 277 (2006) 148–156, <https://doi.org/10.1016/j.memsci.2005.10.025>.
- [27] P.J. Griffin, G.B. Salmon, J. Ford, K.I. Winey, Predicting the solution morphology of a sulfonated pentablock copolymer in binary solvent mixtures, *J. Polym. Sci., Part B: Polym. Phys.* 54 (2016) 254–262, <https://doi.org/10.1002/polb.23914>.
- [28] K.P. Mineart, X. Jiang, H. Jinnai, A. Takahara, R.J. Spontak, Morphological investigation of midblock-sulfonated block ionomers prepared from solvents differing in polarity, *Macromol. Rapid Commun.* 36 (2015) 432–438, <https://doi.org/10.1002/marc.201400627>.
- [29] F.H. Akhtar, H. Vovushua, L.F. Villalobos, R. Shevate, M. Kumar, S.P. Nunes, U. Schwingenschlogl, K.V. Peinemann, Highways for water molecules: interplay between nanostructure and water vapor transport in block copolymer membranes, *J. Membr. Sci.* 572 (2019) 641–649, <https://doi.org/10.1016/j.memsci.2018.11.050>.
- [30] V. Vasil'Eva, N. Pismenskaya, E. Akberova, K. Nebavskaya, Effect of thermochemical treatment on the surface morphology and hydrophobicity of heterogeneous ion-exchange membranes, *Russ. J. Phys. Chem. A* 88 (2014) 1293–1299, <https://doi.org/10.1134/S0036024414080317>.
- [31] E.Y. Safronova, I.A. Stenina, A.B. Yaroslavl'tsev, The possibility of changing the transport properties of ion-exchange membranes by their treatment, *Petrol. Chem.* 57 (2017) 299–305, <https://doi.org/10.1134/S0965544117040065>.
- [32] O.A. Demina, A.V. Demin, N.P. Gnusin, V.I. Zabolotskii, Effect of an aprotic solvent on the properties and structure of ion-exchange membranes, *Polym. Sci.* 52 (2010) 1270–1282, <https://doi.org/10.1134/S0965544x10120059>.
- [33] C.A. Hu, X.L. Deng, X.C. Dong, Y.Z. Hong, Q.G. Zhang, Q.L. Liu, Rigid crosslinkers towards constructing highly-efficient ion transport channels in anion exchange membranes, *J. Membr. Sci.* 619 (2021), 118806, <https://doi.org/10.1016/j.memsci.2020.118806>.
- [34] A. Münchinger, K.-D. Kreuer, Selective ion transport through hydrated cation and anion exchange membranes I. The effect of specific interactions, *J. Membr. Sci.* 592 (2019), 117372, <https://doi.org/10.1016/j.memsci.2019.117372>.
- [35] Y. Ji, H. Luo, G.M. Geise, Effects of fixed charge group physicochemistry on anion exchange membrane permselectivity and ion transport, *Phys. Chem. Chem. Phys.* 22 (2020) 7283–7293, <https://doi.org/10.1039/d0cp00018c>.
- [36] A. Amel, N. Gavish, L. Zhu, D.R. Dekel, M.A. Hickner, Y. Ein-Eli, Bicarbonate and chloride anion transport in anion exchange membranes, *J. Membr. Sci.* 514 (2016) 125–134, <https://doi.org/10.1016/j.memsci.2016.04.027>.
- [37] C. Wang, B.M. Mo, Z.F. He, X.F. Xie, C.X. Zhao, L.Q. Zhang, Q. Shao, X.K. Guo, E. K. Wujcik, Z.H. Guo, Hydroxide ions transportation in polynorbornene anion exchange membrane, *Polymer* 138 (2018) 363–368, <https://doi.org/10.1016/j.polymer.2018.01.079>.
- [38] E.I. Belova, G.Y. Lopatkova, N.D. Pismenskaya, V.V. Nikonenko, C. Larchet, G. Pourcelly, Effect of anion-exchange membrane surface properties on mechanisms of overlimiting mass transfer, *J. Phys. Chem. B* 110 (2006) 13458–13469, <https://doi.org/10.1021/jp062433f>.
- [39] T. Luo, S. Abdu, M. Wessling, Selectivity of ion exchange membranes: a review, *J. Membr. Sci.* 555 (2018) 429–454, <https://doi.org/10.1016/j.memsci.2018.03.051>.
- [40] M. Tedesco, H.V.M. Hamelers, P.M. Biesheuvel, Nernst-Planck transport theory for (reverse) electro dialysis: II. Effect of water transport through ion-exchange membranes, *J. Membr. Sci.* 531 (2017) 172–182, <https://doi.org/10.1016/j.memsci.2017.02.031>.
- [41] K.F.L. Hagesteijn, S.X. Jiang, B.P. Ladewig, A review of the synthesis and characterization of anion exchange membranes, *J. Mater. Sci.* 53 (2018) 11131–11150, <https://doi.org/10.1007/s10853-018-2409-y>.
- [42] C.M. Hansen, *Hansen Solubility Parameters: a User's Handbook*, CRC press, 2007.
- [43] M. Hristova, T. Donchev, D. Kolev, I. Baloch, H. Georgiev, Parameter's estimate in Wilson equation, *Int. Electron. J. Pure Appl. Math.* 9 (2015) 29–35, <https://doi.org/10.12732/iejpam.v9i1.4>.
- [44] J. Gaube, J.M. Sørensen, W. Arlt, Liquid-liquid equilibrium data collection, in: *der Reihe: Dechema Chemistry Data Series, vol. V, Wiley Online Library, 1982. Part 1: Binary Systems*.
- [45] W. Chen, M. Mandal, G. Huang, X. Wu, G. He, P.A. Kohl, Highly conducting anion-exchange membranes based on cross-linked poly(norbornene): ring opening metathesis polymerization, *ACS Appl. Energy Mater.* 2 (2019) 2458–2468, <https://doi.org/10.1021/acsaem.8b02052>.
- [46] J. Yanmei, L. Haihui, W. Ning, H. Lichen, Z. Xing-Xiang, Dispersibility and chemical bonds between multi-walled carbon nanotubes and poly (ether ether ketone) in nanocomposite fibers, *Mater. Chem. Phys.* 135 (2012) 948–956, <https://doi.org/10.1016/j.matchemphys.2012.05.083>.
- [47] K.P. Mineart, B. Lee, R.J. Spontak, A solvent-vapor approach toward the control of block ionomer morphologies, *Macromolecules* 49 (2016) 3126–3137, <https://doi.org/10.1021/acs.macromol.6b00134>.
- [48] T. Konishi, D. Okamoto, T. Tadokoro, Y. Kawahara, K. Fukao, Y. Miyamoto, Origin of SAXS intensity in the low-q region during the early stage of polymer crystallization from both the melt and glassy state, *Phys. Rev. Materials* 2 (2018), 105602, <https://doi.org/10.1103/PhysRevMaterials.2.105602>.
- [49] T.P. Pandey, A.M. Maes, H.N. Sarode, B.D. Peters, S. Lavina, K. Vezzu, Y. Yang, S. D. Poynton, J.R. Varcoe, S. Seifert, M.W. Liberatore, V. Di Notob, A.M. Herring, Interplay between water uptake, ion interactions, and conductivity in an e-beam grafted poly(ethylene-co-tetrafluoroethylene) anion exchange membrane, *Phys. Chem. Chem. Phys.* 17 (2015) 4367–4378, <https://doi.org/10.1039/c4cp05755d>.
- [50] Q.J. Duan, S.H. Ge, C.Y. Wang, Water uptake, ionic conductivity and swelling properties of anion-exchange membrane, *J. Power Sources* 243 (2013) 773–778, <https://doi.org/10.1016/j.jpowsour.2013.06.095>.
- [51] Y.W. Zheng, U. Ash, R.P. Pandey, A.G. Ozioko, J. Ponce-Gonzalez, M. Handl, T. Weissbach, J. Varcoe, S. Holdcroft, M.W. Liberatore, R. Hiesgen, D.R. Dekel, Water uptake study of anion exchange membranes, *Macromolecules* 51 (2018) 3264–3278, <https://doi.org/10.1021/acs.macromol.8b00034>.
- [52] Y. Liu, B.Z. Zhang, C.L. Kinsinger, Y. Yang, S. Seifert, Y.S. Yan, C.M. Maupin, M. W. Liberatore, A.M. Herring, Anion exchange membranes composed of a poly(2,6-dimethyl-1, 4-phenylene oxide) random copolymer functionalized with a bulky phosphonium cation, *J. Membr. Sci.* 506 (2016) 50–59, <https://doi.org/10.1016/j.memsci.2016.01.042>.
- [53] M.J. Kadhim, M.I. Gamaj, Estimation of the diffusion coefficient and hydrodynamic radius (Stokes radius) for inorganic ions in solution depending on molar conductivity as electro-analytical technique—a review, *J. Chem. Rev.* 2 (2020) 182–188, <https://doi.org/10.22034/JCR.2020.106910>.
- [54] Y. Li, S. Yuan, Y. Xia, W. Zhao, C.D. Easton, C. Selomulya, X.W. Zhang, Mild annealing reduced graphene oxide membrane for nanofiltration, *J. Membr. Sci.* 601 (2020), 117900, <https://doi.org/10.1016/j.memsci.2020.117900>.
- [55] C.P. Kelly, C.J. Cramer, D.G. Truhlar, SM6: a density functional theory continuum solvation model for calculating aqueous solvation free energies of neutrals, ions, and solute-water clusters, *J. Chem. Theor. Comput.* 1 (2005) 1133–1152, <https://doi.org/10.1021/ct050164b>.
- [56] V. Pavluchkov, I. Shefer, O. Peer-Haim, J. Blotvogel, R. Epsztein, Indications of ion dehydration in diffusion-only and pressure-driven nanofiltration, *J. Membr. Sci.* 648 (2022), 120358, <https://doi.org/10.1016/j.memsci.2022.120358>.
- [57] S.B. Sigurdardottir, R.M. DuChanois, R. Epsztein, M. Pinedo, M. Elimelech, Energy barriers to anion transport in polyelectrolyte multilayer nanofiltration membranes: role of intra-pore diffusion, *J. Membr. Sci.* 603 (2020), 117921, <https://doi.org/10.1016/j.memsci.2020.117921>.
- [58] K. Cooper, Characterizing through-plane and in-plane ionic conductivity of polymer electrolyte membranes, *ECS Trans.* 41 (2011) 1371.
- [59] B. Chen, P. Mardle, S. Holdcroft, Probing the effect of ionomer swelling on the stability of anion exchange membrane water electrolyzers, *J. Power Sources* 550 (2022), 232134, <https://doi.org/10.1016/j.jpowsour.2022.232134>.
- [60] M.J. Park, K.H. Downing, A. Jackson, E.D. Gomez, A.M. Minor, D. Cookson, A. Z. Weber, N.P. Balsara, Increased water retention in polymer electrolyte membranes at elevated temperatures assisted by capillary condensation, *Nano Lett.* 7 (2007) 3547–3552, <https://doi.org/10.1021/nl072617l>.
- [61] N.W. Li, M.D. Guiver, Ion transport by nanochannels in ion-containing aromatic copolymers, *Macromolecules* 47 (2014) 2175–2198, <https://doi.org/10.1021/ma402254h>.